Materials Advances

ROYAL SOCIETY OF CHEMISTRY

PAPER

View Article Online
View Journal | View Issue

Cite this: *Mater. Adv.*, 2025, 6, 3253

Toward highly efficient protonic electrolysis cells for large-scale hydrogen production at moderate temperatures†

Leonard Kwati, *[acd] Kuninori Miyazaki,[b] Christian Dellen,[c] Mariya E. Ivanova,[c] Wendelin Deibert,[c] Julia Wolter,[c] Wilhelm A. Meulenberg,[c] Olivier Guillon,[c] Veeramani Vediyappan,[d] Tatsumi Ishihara[ad] and Hiroshige Matsumoto[ad]

Ceramic proton-conducting electrolytes are highly appealing for large-scale hydrogen production *via* steam electrolysis at low to moderate temperatures. However, processing such electrolytes for industrial purposes poses several challenges. Our research demonstrates an effective tape-casting route that produces flat, planar $BaZr_{0.44}Ce_{0.36}Y_{0.2}O_{3-\delta}$ protonic half-cells with impressive dimensions of up to 50 mm × 50 mm. The cells are constructed using NiO-$SrZr_{0.5}Ce_{0.4}Y_{0.1}O_{3-\delta}$ as the fuel electrode, which ensures minimal warping and no cracks in the end-fired state. The electrolyte is dense and gas-tight after co-firing at 1300 °C and achieves a He leakage rate well within the threshold necessary for cell operation ($\sim 5 \times 10^{-5}$ hPa dm^3 s^{-1} cm^2)$^{-1}$. Using $B_{0.5}La_{0.5}CoO_{3-\delta}$ as the steam electrode, the cell achieves an electrolysis voltage of 1.3 V at a current density of 1.37 A cm^{-2} at 600 °C. Moreover, they also exhibit high durability, lasting over 1000 hours of continuous hydrogen generation with no observable degradation, which is a testament to their reliability. In addition, scanning electron microscopy paired with energy-dispersive X-ray spectroscopy, Raman spectroscopy, and X-ray diffraction were employed to examine the structural changes in the half-cells after sintering at different temperatures. It is apparent from the latter techniques that upon sintering above 1350 °C, the electrolyte undergoes evident structural changes with new defects that affect the perovskite host. Finally, our work paves the way for the cost-effective fabrication of planar proton-conducting electrolysis cells.

Received 10th January 2025,
Accepted 6th April 2025

DOI: 10.1039/d5ma00028a

rsc.li/materials-advances

1. Introduction

Hydrogen is a versatile energy carrier perceived widely as indispensable for a future energy transition.[1] Currently, most hydrogen (~95.5%) produced today is by steam reforming of natural gas because of the high efficiency (60–85%) and the low price of natural gas, mostly without integrating technologies to reduce or mitigate CO_2 emissions.[1,2] Electrolytic hydrogen production methods like alkaline and proton exchange membrane electrolysis are suitable clean options and have achieved a certain degree of technological maturity. Still, the high cost of these technologies continues to limit their market share. As a result, less than 0.1% of dedicated hydrogen produced globally comes from these approaches.[3] This underscores the urgent need for low-cost, efficient hydrogen production approaches, which our research aims to address.

Solid oxide steam electrolysis (SOECs) at moderate temperatures (300–600 °C) offers excellent prospects for efficient and cost-effective large-scale hydrogen production,[4,5] depending on the source of the electricity used. This temperature domain also allows seamless heat integration options and non-noble materials, which will benefit cost. Furthermore, the overpotential is lower, as the electrolysis reactions are favored by kinetics at higher temperatures. It is also worth noting that SOECs can operate in reverse mode as fuel cells, enabling the conversion of hydrogen back into electricity. This sets them apart from alkaline and PEM electrolysis, allowing them to provide grid-balancing services when paired with hydrogen storage facilities.[1,4,6]

Proton-conducting ceramic (PCC) solid-oxide represents viable, moderate-temperature electrolytes for these devices, given their high ionic conductivity and inherent advantages

[a] *Center for Energy Systems Design (CESD), International Institute for Carbon Neutral Energy Research (WPI-I2CNER), Kyushu University, 744 Motooka, Nishiku, Fukuoka 819-0395, Japan. E-mail: kwati@i2cner.kyushu-u.a.jp; Tel: +81-092-802-6706*
[b] *Strategic Institute of Technology and Research Center, 992-1 Nishioki, Himeji, Hyogo 671-1292, Japan*
[c] *Institute of Energy Materials and Devices (IMD) Materials Synthesis and Processing (IMD-2), Forschungszentrum Jülich GmbH, Wilhelm-Johnen-Straße 52428, Germany*
[d] *International Institute for Carbon Neutral Energy Research (WPI-I2CNER), Kyushu University, 744 Motooka, Nishiku, Fukuoka 819-0395, Japan*

† Electronic supplementary information (ESI) available. See DOI: https://doi.org/10.1039/d5ma00028a

in the gas flow configuration over traditional solid oxide cells in which the electrolyte is an oxygen ion conductor.[7–11] Protonic conductivity in this class of materials relies on the partial filling of vacant oxygen sites by water to yield mobile proton interstitials bound to lattice oxide ions. The inserted protons subsequently exhibit relatively high mobility and give rise to the significant protonic conductivity observed.[11,12] State-of-the-art protonic electrolytes comprise acceptor-doped perovskite oxides within the $Ba(Zr_xCe_{1-x})Y_yO_{3-\delta}$ solid solution series.[9] Compositions such as $BaZr_{0.4}Ce_{0.4}Y_{0.1}Yb_{0.1}O_{3-\delta}$ (BZCYYb411)[8] $BaCe_{0.55}Zr_{0.3}Y_{0.15}O_{3-\delta}$ (BCZY3), $BaZr_{0.1}Ce_{0.7}Y_{0.2}O_{3-\delta}$ (BZCY172),[13] and $BaZr_{0.1}Ce_{0.7}Y_{0.1}Yb_{0.1}O_{3-\delta}$ (BZCYYb1711)[14,15] are among the most reported within this series. In addition, recent progress in developing suitable air electrode materials explicitly tailored for these electrolytes[16] has made it possible to achieve high-performing proton conducting fuel cells (PCFC),[8,10,17] substantially lower cell voltages at higher current densities, and high current efficiencies in protonic ceramic electrolysis cells (PCEC).[18,19] However, to date, most reported cells have been realized mainly with laboratory-scale button cells having a relatively limited cell size (less than 3 cm^2) and electrode surface area (0.2–0.5 cm^2). Only a few systematic investigations have focused on scale-up efforts.[20,21] This is due to the challenges of scaling up proton-conducting ceramic solid oxide.[22] Besides the desirable high current densities of the small-size button cells, in many instances exceeding (in magnitude) 1.0 A cm^{-2} even at 600 °C under a thermo-neutral operating voltage of ~1.3 V, concurrent hydrogen generation rates are scarce, let alone over several continuous hours of operation with only a few exceptions.[23] Long-term durability lasting hundreds of hours with simultaneous successive hydrogen generation is greatly needed to advance PCEC technology.[14]

As a technical issue, these electrolyte types generally require high sintering temperatures (≥1500 °C) and a longer duration to densify completely. Such high temperatures can increase the overall processing cost in the fabrication process and cause the evaporation of essential elements like barium, leading to off-stoichiometry and decreasing ionic conductivity, which is unfriendly to the device's performance.[7] Recent studies have also shown that the sintering temperature of such electrolytes in bilayer structures can be reduced when in contact with a NiO-containing electrode, as NiO acts as an inherent sintering aid.[8–10] To attain the desired microstructures in such a bilayer consisting of a porous electrode and dense electrolyte, the sintering schedule must be carefully designed, considering the shrinkage of both layers. Moreover, similar to SOEC technology, there are significant challenges in scaling up flat, robust, and durable proton conducting electrochemical cells (PCECs). These devices are complex multilayer structures with varying compositions and microarchitectures, making them susceptible to warping during sintering. This warping behavior often leads to poor sealing and imposes additional mechanical stress on the cells during operation. Notably, the degree of warping tends to increase with larger cell sizes. Therefore, the cells' size and flatness are critical factors in the design of PCEC stacks, which are essential for commercial hydrogen production applications. Thus, careful control over chemical incompatibilities between the cell components[20] is necessary to avoid cracked, pinhole defects, and performance loss.

This study demonstrates a cost-effective tape casting and screen-printing route to fabricate flat planar cathode-supported PCEC cells with NiO-$SrZr_{0.5}Ce_{0.4}Y_{0.1}O_{3-\delta}$ (NiO-SZCY541) as the negative electrode. By carefully controlling powder properties and slurry formulations, $BaZr_{0.44}Ce_{0.36}Y_{0.2}O_{3-\delta}$ (BZCY44362) half-cells of dimensions up to 50 mm × 50 mm × 0.5 mm with diminished warping and no cracks in the end-fired state have been fabricated. Minimal strontium segregation from the NiO-SZCY541 electrode during sintering significantly influences the electrolyte densification and potentially mitigates the half-cell warped behavior. Furthermore, scanning electron microscopy in combination with energy-dispersive X-ray spectroscopy, Raman spectroscopy, and X-ray diffraction were used to analyze the structural modifications of the half-cells upon sintering at varying temperatures. It is apparent from the latter techniques that upon sintering above 1350 °C, the electrolyte undergoes evident structural changes with new defects that affect the perovskite host.

2. Experimental section

2.1. Materials and structural characterizations

The electrolyte and electrode materials $BaZr_{0.44}Ce_{0.36}Y_{0.2}O_{3-\delta}$ (BZCY44362), $SrZr_{0.5}Ce_{0.4}Y_{0.1}O_{3-\delta}$ (SZCY541) and $Ba_{0.5}La_{0.5}CoO_3$ (BLC55) were synthesized following previously reported procedure.[11] Large quantities of BZCY44362 and SZCY541 powders were also purchased from KUSAKA RARE METAL PRODUCTS Co. Ltd, Japan, with similar powder properties as the synthesized. Powder X-ray diffraction patterns of the former and latter powders were analyzed for phase purity using a Rigaku X-ray diffractometer at room temperature with Cu-Kα radiations at 40 kV and 40 mA. Diffraction patterns were obtained in the 2θ range between 10° and 80° with a step size of 0.02° and a scan rate of 2° min^{-1}. Powder morphology, as well as the surfaces and polished cross-sections of half-cells, were observed by field emission-scanning electron microscopy SEM (Hitachi High-Technologies SU8000 equipped with energy-dispersive X-ray spectroscopy) (Oxford INCA energy 300 EDS). SEM and EDS cross-sectional analysis samples are prepared by a conventional cold embedding method, using a liquid epofix resin and a hardener, mixed in a 9 : 1 ratio, with 0.4 wt% methyl ethyl ketone added to improve the viscosity. Raman spectroscopy mappings were taken using a Renishaw inVia Qontor confocal Raman microscope. The system was used to gather Raman mappings of the sample surfaces and polished cross-section samples. All the Raman measurements were conducted with a green laser (532 nm wavelength) and a 2400 l mm^{-1} grating.

2.2. Slurry preparation and cell fabrication

Half-cells were fabricated using a scalable and well-established sequential tape-casting route with a KARO cast 300-7 micro-tape casting device (KMS Automation GmbH Germany). The substrate support slurry consisted of commercial NiO powder

(Vogler, raw material) and SZCY541 (NiO, SZCY541, at a weight ratio of 60 : 40) dispersed in an ethanol and methyl ethyl ketone (66 : 34%) mixture together with Nuosperse FX9086 (1%) (Elementis Specialties, Inc., London, UK) as the dispersing agent. Furthermore, polyvinyl butyral (Butvar PVB-98 (4.66%), Solutia Inc., St. Louis, MO, USA) and Solusolv 2075 (Solutia Inc., St. Louis, MO, USA) were added as plasticizers, along with polyethyleneglycol PEG 400 (Merck Schuchardt, Hohenbrunn, Germany) serving as a binder (2.33%). The mixture was homogenized in a Thinky vacuum mixer and left to rest for 48 hours to de-air and completely dissolve the binder before casting. The electrolyte slurry was prepared using a previously reported two-step procedure with minor modifications and cast onto a silicone-coated polymeric (polyethylene terephthalate) foil.[2,3] After proper drying at room temperature, a functional NiO-SZCY541 layer (without pore former) was cast directly on top of the electrolyte layer, followed by the support NiO-SZCY541 (with 5 wt% rice starch as pore former) slurry with a six-hour drying interval. This approach guarantees the formation of defect-free electrolyte layers, thanks to the superior surface quality of the foil. The green tapes were then precisely cut to the desired dimensions and sintered at 1300 °C, 1350 °C, and 1400 °C for 5 and 10 hours, respectively. Half-cells measuring 50 × 50 mm^2 and 22 mm diameter with the following configurations BZCY44362|NiO-BZCY44362 (dense layer) |NiO-BZCY44362 (porous)| and BZCY44362|NiO-SZCY541 (dense layer)|NiO-SZCY541 (porous)| were used for characterisation. While flat half-cells of 50 × 50 mm^2 and 22 mm in diameter could be easily produced for the latter configuration, the former could only yield flat half-cells with a diameter of 22 mm. The thickness of the electrolyte was controlled by adjusting the gap between the polymer foil and the doctor blade. The curvature of the half-cells after sintering was measured using a white light topography unit (CT 350, CyberTechnologies, Ingolstadt, Germany). Thermo-gravimetric analysis (TGA) and differential thermal analysis (DTA) coupled with mass spectrometry (MS) were carried out using a Netzsch S.T.A. 409C system to understand the decomposition behavior of the organic additives in both the electrolyte and NiO-based substrate single layers. Measurements were conducted at a maximum temperature of 1000 °C using a heating rate of 5 °C min^{-1} and in a constant flow of nitrogen and oxygen gases at ambient pressure. The warpage/bending behavior of the half-cell was investigated by comparing their shrinkage behavior using a TOMMI plus optical dilatometer (Fraunhofer I.S.C., Würzburg, Germany). The instrument features a furnace with quartz windows, a light source, and a camera. It continuously records images of the sample silhouette during heat treatment, enabling precise determination of shrinkage through careful selection of the sample geometry. To further improve the mechanical properties of the half-cells, the co-cast layers were further compressed by applying a pressure of 8 MPa at 80 °C using a warm press by P/O Weber. The gas tightness of the 50 × 50 mm^2 half-cell was evaluated using helium leakage rate measurements. A mass spectrometer measured gas flow through the half-cell at a pressure difference of 1000 hPa, which was then normalized for an area of 16 cm^2 and a pressure difference of 100 hPa. Finally, a $Ba_{0.5}La_{0.5}CoO_{3-\delta}$ anode slurry was prepared by mixing the powder with terpineol (containing 5 wt% ethylcellulose). This mixture was screen-printed onto the electrolyte surface with an active area of 0.5 (22 mm diameter half-cell) and 1 cm^2 (50 × 50 mm^2 half-cell), achieving a final thickness of ~30 μm after sintering at 800 °C for 1 hour.

2.3. Electrochemical performance of the as-fabricated cells

Electrochemical performance tests were carried out on the as-fabricated single cells. The cells were mounted into ceramic housings and sealed with Pyrex glass for the 22 mm diameter cells and gold frames for the 50 × 50 mm^2 cell configuration. To evaluate the open circuit characteristics, as well as the leakage and impedance spectra of the cells, humidified hydrogen (5% H_2O) was supplied to the fuel side (negative electrode) at a flow rate of 250 mL min^{-1}, while dry air was introduced to the air side (positive electrode) at the same flow rate. In the electrolysis test, the anode of the 22 mm diameter cell from both electrode substrates was supplied with humidified 80 vol% H_2O mixed and 1 vol% O_2/99 vol% Ar/(50 mL min^{-1}) carrier gas. Simultaneously, the cathode was supplied with 1% H_2/Ar 99% (50 mL min^{-1}), maintaining a water vapor pressure of P_{H_2O} = 1.9 × 10^3 Pa. A hygrometer chilled mirror (UHQ-4P, Buck Research Instruments LLC, Tokyo, Japan) monitored the anode inlet's water vapor pressure. Gas lines were heated at 120 °C to prevent the condensation of water vapor. Hydrogen evolution was determined by measuring the increase in hydrogen concentration in the cathode gas outlet by gas chromatography (Varian CP-4900 micro-Gas Chromatograph equipped with a micro-machined Thermal Conductivity Detector (TCD), Agilent Technologies Inc., Tokyo, Japan). Faradaic efficiencies were obtained based on the experimentally measured and theoretical hydrogen generation rates at fixed current densities using the following formula.

$$\mathrm{FE} = \frac{n_{\mathrm{H_2,measured}}}{n_{\mathrm{H_2,theoretical}}} = \frac{n_{\mathrm{H_2,measured}} \times (n \times F)}{J} \times 100(\%)$$

where n_{H_2}, represents the measured hydrogen evolution rate (mol s^{-1}), n is 2, F is the faradaic constant (96 485 C mol^{-1}), and J is the applied current density in (A). Energy efficiency was calculated based on the lower heating value of hydrogen, as shown in the equation below.

$$\mathrm{EE} = \frac{\Delta H_{\mathrm{H_2LHV}} \times n_{\mathrm{H_2,measured}}}{J \times V} = \frac{n_{\mathrm{H_2,measured}} \times (n \times F)}{J \times V} \times 100(\%)$$

where ΔH_{H_2LHV} represent the lower heating value reaction enthalpy for steam electrolysis, which is 241.8 kJ mol^{-1} and V is the corresponding voltage (V). The electrochemical performance of single cells was evaluated using a potentiostat (Bio-Logic, VMP-250) at operating temperatures from 450 to 600 °C. Impedance spectra were measured under open circuit voltage (OCV) in the frequency range from 1 MHz to 0.1 Hz with an AC amplitude of 10 mV. Humidified H_2 (5% H_2O) and air with flow rates of 250 mL m^{-1} were introduced at the cathode and anode of the 50 mm × 50 mm cell, respectively.

3. Results and discussion

3.1. Electrolyte composition and powder properties

Fig. 1. presents a schematic illustration of water splitting using a typical PCEC cell and the as-fabricated 50 mm × 50 mm × 0.5 mm cell. Our group recently discovered a unique proton-conducting composition $BaZr_{0.44}Ce_{0.36}Y_{0.2}O_{3-\delta}$ in the $Ba(Zr_xCe_{10-x})_{0.08}Y_{0.2}O_{3-\delta}$ ($1 \leq x \leq 9$) family, achieved by fixing a cerium/zirconium ratio of 5:4 at the perovskite B-site.[9,11] As a result, the unique composition $BaZr_{0.44}Ce_{0.36}Y_{0.2}O_{3-\delta}$ (BZCY44362) exhibits a high conductivity (10.1 mS cm^{-1} at 500 °C in wet 1% H_2), excellent chemical stability under steam and CO_2, as well as satisfactory processability.[9] This target composition with modified versions and a composite NiO-SZCY541 were chosen for the half-cell fabrication *via* an inverse tape casting approach.[20] Choosing a suitable starting powder is crucial to ceramic processing, as it significantly influences the quality of the tapes and their sintering properties. The BZCY44362 electrolyte and SZCY541 powder properties used were thus first ensured *via* a two-step calcination process at 900 and 1200 °C, respectively, with subsequent milling (in ethanol).

This treatment leaves both materials with a comparably low particle size distribution d_{50} of 0.68 and 0.70 μm and specific surface area (A_{spec}) of 5.1 and 4.7 $m^2\ g^{-1}$, respectively, which are satisfactory for making optimal slurries for tape casting and providing the necessary driving force for densification during sintering. Fig. S1 (ESI†) presents SEM images of the powders and particle size distribution used in the slurry for casting. Sequential tape casting was used to fabricate the layers, after which green tapes were cut into 65 × 65 mm^2 using a scalpel blade for co-sintering to obtain an integrated electrolyte/NiO composite ceramic known as half-cell.[20] Deformation and warpage of the half-cells were controlled by adequately optimizing the binder, plasticizer, and dispersant amount. The sintering process of tape-cast layers also plays a vital role in fabricating high-quality flat ceramic components. The burn-out behavior of the organic additives in the tape-cast layers has been discussed in our previous manuscripts and briefly in the subsequent section. A slow ramp rate of 1 °C min^{-1} was used for sintering, with holding temperatures of 300 °C and 600 °C maintained for 30 minutes. After this, a 2 °C min^{-1} ramp rate was employed, as shown below. Flat, 50 × 50 mm^2 half-cells, after sintering, were routinely obtained by this procedure, corresponding to 23.1% shrinkage along the axes. We also noted that a cathode substrate support of 450 μm in the end-fired state was sufficient to induce mechanical strength and mitigate the overall half-cell curvature. Table S1 (ESI†) presents suitable processing parameters for the green tape fabrication. The NiO-SZCY541-based half-cells are flat and achieve a dense, gas-tight BZCY44362 electrolyte layer after co-sintering at 1300 °C for 5 hours, which is about 200 °C lower than required for the electrolyte alone. In contrast, the same electrolyte composition did not densify enough when placed on the NiO-BZCY44362 electrode substrate at 1350 °C, probably because of Ba loss and yttrium displacement from the perovskite B-site into the A-site resulting in lattice shrinkage, which probably deteriorates the electrolyte densification. The mechanism of barium evaporation deteriorating the electrolyte sintering is still not precise. Based on observation, however, the latter half-cell appeared dense after sintering at 1450 °C but showed significant edge warping in the 50 × 50 mm^2 size configuration. Flat half-cells of this size could not be made using the NiO-BZCY44362 electrode substrate, so the dimensions were reduced to 22 mm in diameter with a 450 μm support thickness for cell operation and comparison. A sintering temperature of 1500 °C and a dwell time of 3 hours were thus required. This high temperature also triggers yttrium precipitation around the nickel oxide grain vicinity, which may result in a stoichiometric imbalance, as discussed in the subsequent section. This imbalance can reduce the concentration of oxygen vacancies in the material, negatively affecting the electrolyte's conductivity and, consequently, the cell's performance. For such half-cells, the structural and compositional uniformity of the cement electrode and the aligned shrinkage behaviors of the electrode and electrolyte layers are critical for a successful scale-up. Any differences in shrinkage from temperature changes can cause flaws in the support's biaxial constraints, leading to severe issues like pinholes, cracks, and delamination in the half-cells after sintering. These problems are also likely to worsen as the half-cell size increases. To further comprehend how the NiO-SZCY541 composite promotes the densification of the electrolyte, optical dilatometry was used to investigate the lateral shrinkage behavior of both the single electrolyte and bi-layers. Fig. 2(a) compares the lateral shrinkage of the single BZCY44362 layer, the NiO-BZCY44362-BZCY44362 bilayer, and the NiO-SZCY541-BZCY44362 bilayer. The NiO-SZCY541 bilayer shows a higher shrinkage of 34%, compared to 26% for the NiO-BZCY44362 half-cells. This indicates the latter bilayer should, in principle, assist and improve the

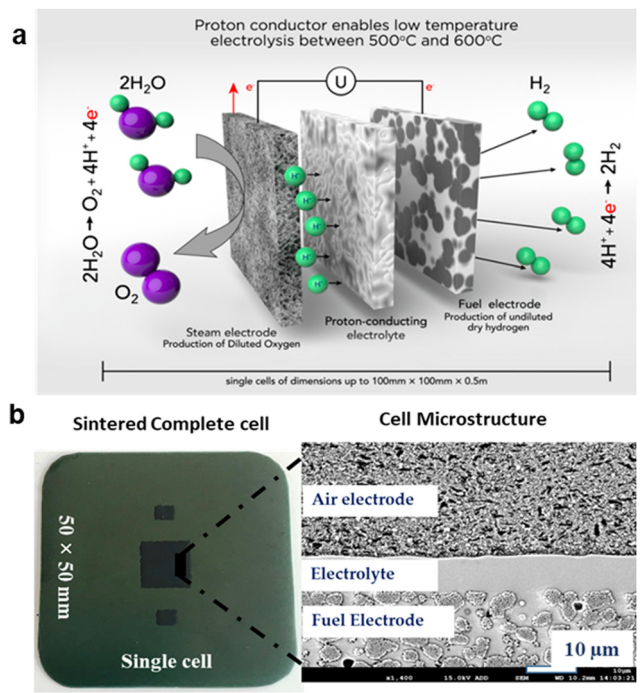

Fig. 1 (a) Schematic illustration of a steam proton conducting electrolysis cell (PCEC). (b) BZCY44362-based cell in the end-fired state with the microstructure after reduction.

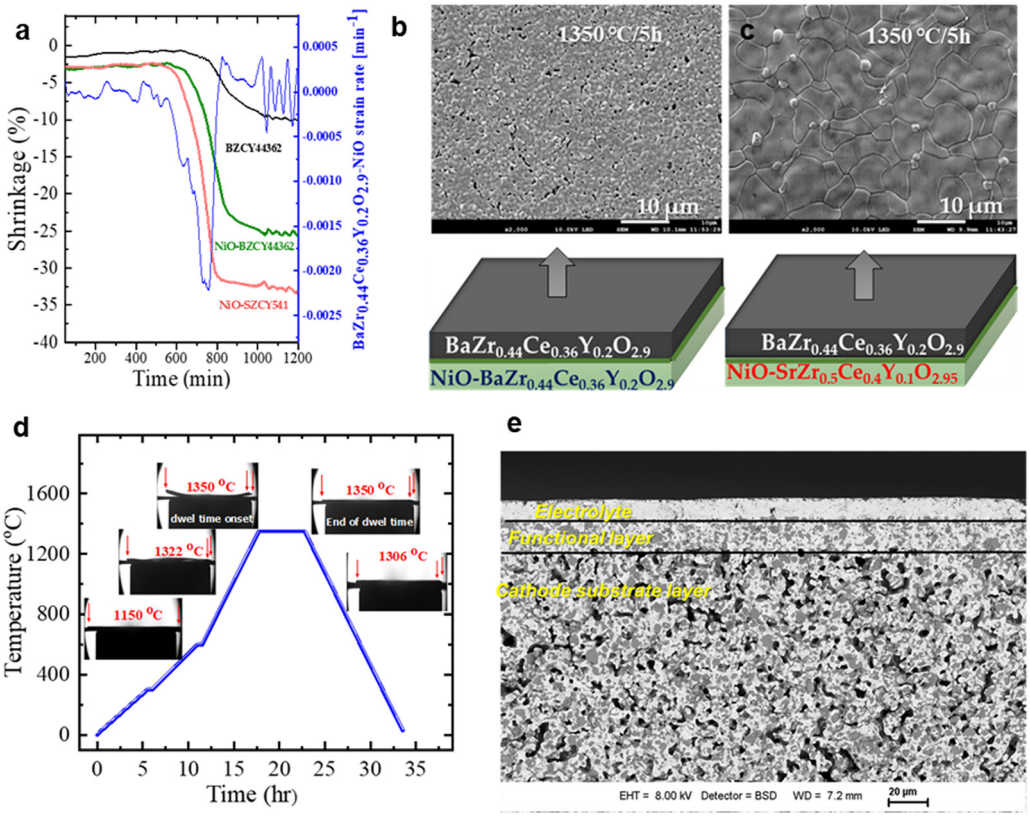

Fig. 2 (a) Shrinkage behavior of the BZCY44362 electrolyte, BZCY44362|NiO-BZCY44362 and BZCY44362|NiO-SZCY541 bi-layers determined by optical dilatometry, at a heating rate of 2 °C min^{-1}. (b) SEM image of BZCY44362 surface view on NiO-BZCY44362 electrode (c) SEM image of BZCY44362 surface view on NiO-SZCY541 after sintering at 1350 °C (d) sintering of the NiO-SZCY541 based half-cell performed under optical dilatometer, showcasing the sintering profile, and behavior of the 50 × 50 mm^2 size configuration with temperature and time. (e) SEM image of a polished cross-section of the fabricated half-cell.

sintering activity of the electrolyte layer. In comparison, the BZCY44362 single layer shrunk only by ~10%. This is expected since the layer has less organic content and finer particle size. Fig. 2(b) and (c) also compare the surface microstructural view of the same electrolyte composition on both electrode substrates. Fig. 2(c) clearly shows that the NiO-SZCY541-based electrode significantly impacts sintering and grain growth, as indicated by the noticeable differences in grain size and relative density. In contrast, the NiO-BZCY44362-based half-cell (Fig. 2(b)) remains porous even after being sintered at 1350 °C for 5 hours. Thus, the NiO-SZCY541 electrode substrate not only facilitates sintering but also aids in densifying the electrolyte and promoting grain growth, which allows for reduced processing temperatures. Furthermore, Helium leak rate tests performed on the 50 × 50 mm^2 NiO-SZCY541 base half-cell configuration after sintering at 1300 °C for 5 hours indicate an average leak rate of ~5 × 10^{-5} hPa dm^3 (s cm^2)$^{-1}$, which falls well within the acceptable range for high-quality gas-tight electrolytes used in cell operation.

Recent literature suggests that the fundamental mechanism involved in the sintering of barium-based electrolytes is through the formation of a BaY_2NiO_5 transient phase, which is formed at the electrode and supplied to the electrolyte during sintering to aid the process. While this is recognized, it may not be the primary mechanism in the present study.

3.2. Warpage behavior during heating and microstructure of sintered half-cells

Ensuring gas tightness in the electrolyte layer and maintaining half-cell flatness during co-sintering are imperative for a successful scale-up of PCECs with the desired microstructure. An optical dilatometer was utilized to better understand the bending and wrapping behavior of the half-cells during the sintering process. Selected images of the half-cell configuration measuring 50 mm × 50 mm, with the electrolyte side facing upward at various temperatures, are displayed in Fig. 2(d). Initially, the half-cells bend concave downward during the organic burnout stage of heating. After burnout, they return to a flat shape around 1000 °C, which remains stable until approximately 1300 °C. This behavior is consistent with the NiO-BZCY44362-based half-cells (though they turn to flatten at 1500 °C). At this temperature, the electrolyte side densifies more rapidly, causing the half-cell to bend concave upward until around 1350 °C. After this, the half-cells flatten again and maintain this shape while cooling down. STEM-EDS analysis was performed on the obtained half-cells to gain insights into their microstructure after sintering. Fig. 2(e) shows a typical half-cell cross-section featuring a thin ~10-μm dense electrolyte layer, which should allow proton permeation and prevent gas crossovers. A uniform

~15-μm fuel electrode functional layer that adheres well to the electrolyte and a ~430 μm porous support to facilitate gas diffusion for optimal performance. Fig. 3(a) also shows a high-angle annular dark-field (HAADF) STEM analysis of a cross-sectional lamella from the BZCY44362|NiO-BZCY4436 electrode interface sintered at 1500 °C.

It illustrates the elemental distributions of barium (Ba), zirconium (Zr), cerium (Ce), yttrium (Y), and nickel (Ni). The Y maps reveal prominent Y-rich regions that align with the Y_2O_3 phases observed in the X-ray diffraction pattern in Fig. 3(b). This observation is consistent with similar findings reported in the literature.[11,20,24] In contrast, Y_2O_3 phases are rarely observed or utterly absent in the BZCY44362|NiO-SZCY541 half-cell sintered at 1350 °C, as shown in Fig. 3(c). Furthermore, the selected area electron diffraction (SAED) in Fig. 3(d) shows lattice fringes and prominent lattice planes attributed to orthorhombic SZCY541,[24] initially present only in the substrate layer.

Moreso, EDS elemental maps of the cross-section of the latter half-cell shown in Fig. S4 (ESI†) reveal that Sr is predominantly present and uniformly distributed throughout the BZCY44362 electrolyte layer. The investigation into the precise amount of incorporated Sr is ongoing. As discussed, using the NiO-SZCY541 electrode substrate minimizes deformation and warpage, resulting in consistently flat half-cells measuring 50 mm × 50 mm. While the precise cause of this effect remains unclear and is still under investigation, post-sintering measurements taken with a white light topography unit indicate an approximate flatness of 0.2 mm, as shown in Fig. 4. It is likely that strontium diffusion from the latter substrate to the electrolyte layer compensates for some of the barium loss, which may help mitigate the deformation and warpage of the half-cells.

3.3. Steam electrolysis performance

The performances of single cells fabricated with NiO-BZCY44362 or NiO-SZCY541 electrode cement were evaluated

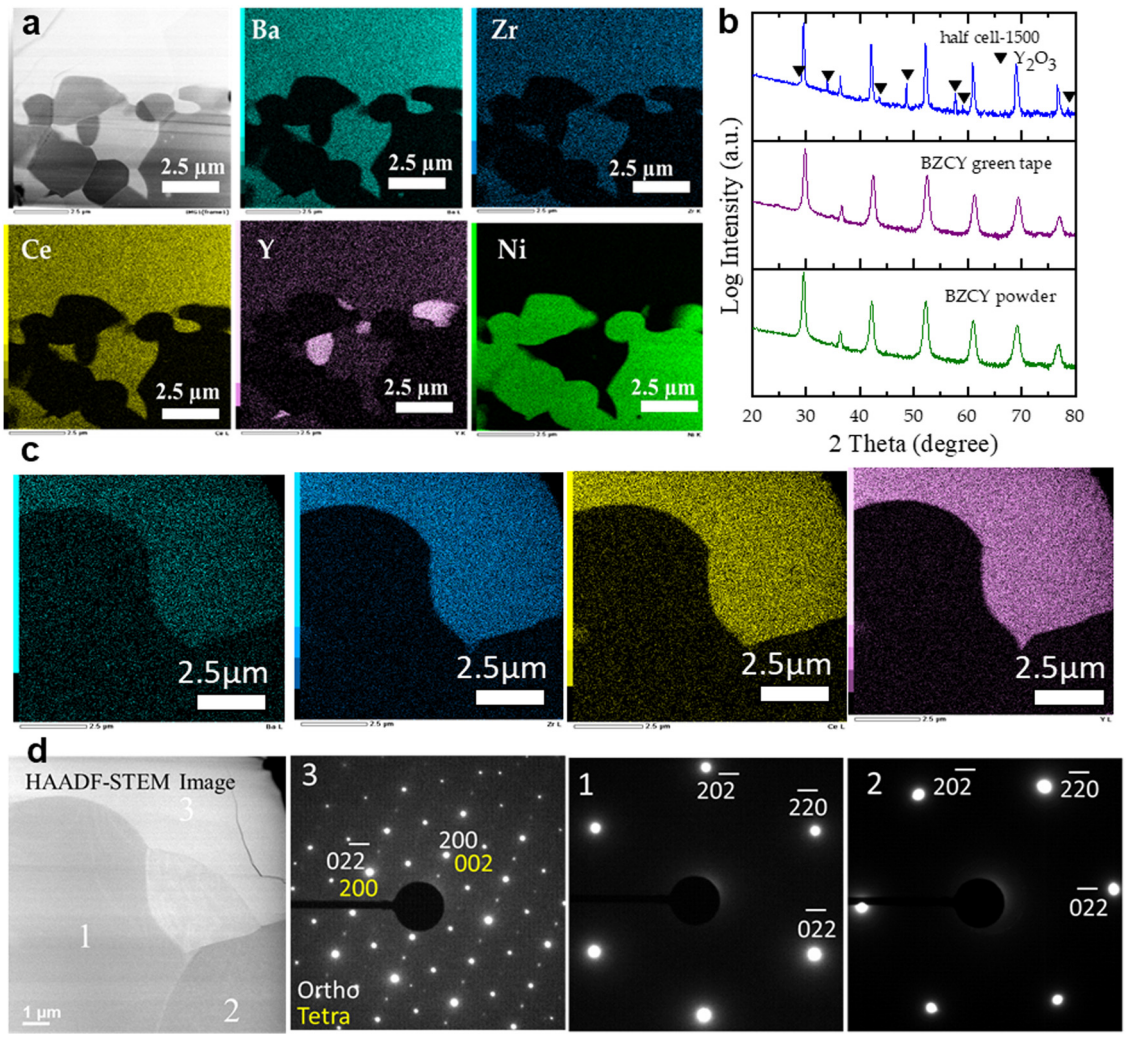

Fig. 3 (a) HAADF micrograph of a cross-sectional lamella of BZCY44362|NiO-BZCY44362 electrode interface with corresponding EDS maps of Ba, Zr, Ce, Y, Ni. (b) Room-temperature X-ray diffraction patterns of BZCY44362 powder, green tape, and the half-cell after sintering at 1500 °C. (c) HAADF micrograph of the BZCY44362/NiO-SZCY541 interface with corresponding EDS maps of Ba, Zr, Ce, Y (d) selected-area electron diffraction pattern with Miller indices and labeled crystallographic direction for Ni and SZCY541.

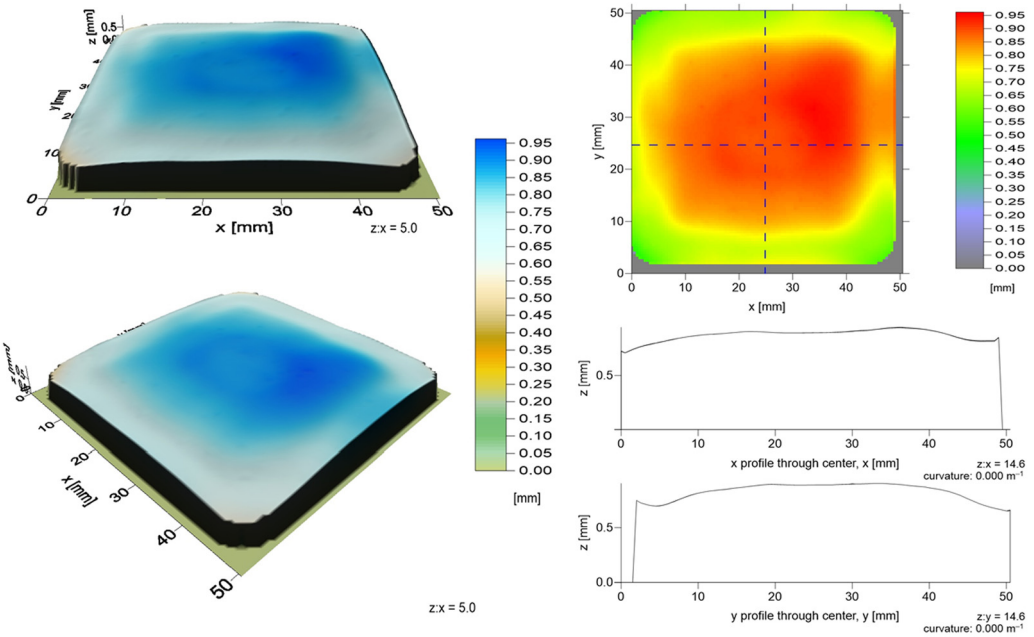

Fig. 4 Curvature and surface flatness of the as-fabricated 50 mm × 50 mm planar protonic electrolysis half-cells with the configuration $BaZr_{0.44}Ce_{0.36}Y_{0.2}O_{3-\delta}$,|NiO-$SrZr_{0.5}Ce_{0.4}Y_{0.1}O_{3-\delta}$ after sintering at 1350 °C/5 h, evaluated by white-light topography measurement.

within the 600–450 °C temperature range. Fig. 5(a) and (b) illustrate the open-circuit voltage (OCV) profile of NiO reduction at varying H_2 concentrations and temperatures on the 22 mm diameter cell with a 0.5 cm^2 electrode area. The results for both cell configurations are similar and closely align with those calculated using the Nernst equation.

The minor differences can be attributed to partial hole conductivity in the electrolyte, consistent with other literature reports. Additionally, the OCVs for the larger 50 × 50 mm^2 NiO-SZCY541-based cell reached 1.09 V at a temperature of 600 °C, indicating that there was also no apparent electronic or gas leakage. Fig. 5(c) depicts current–voltage (*I–V*) curves for the BZCY44362 (10 μm)|NiO-BZCY44362 and BZCY44362 (10 μm)||NiO-SZCY541 based cell measured at 600 °C, under a controlled supply of humidified 1% O_2/99% Ar and 80% H_2O to the air electrode and 1% H_2/Ar 99% at the fuel electrode as the sweep gas. The cell based on BZCY44362 (∼10 μm)|NiO-BZCY44362 achieved an electrolysis current density of 1 A cm^{-2} at 600 °C, with an overpotential of 1.2 V. In contrast, the BZCY44362 (∼10 μm)|NiO-SZCY541 cell also achieved the same current density but with a significantly lower overpotential of only 0.59 V. The performance of the latter cell improves when an electrolyte approximately 8 μm thick is used. At temperatures of 600, 550, 500, and 450 °C, the cell produces electrolysis voltages of 1.3 V at current densities of approximately 1.37, 0.98, 0.5, and 0.22 A cm^{-2}, respectively, Fig. 5(d) and Fig. S6 (ESI†), which are among the best-reported performances at such low temperatures for similar electrolyte composition[8,10,17,25] Fig. 6(d) and Table S3 (ESI†). For example, at 500 °C, Choi *et al.*[8] showed a current density of 0.5 A cm^{-2} at 1.4 V, while Ding *et al.*[17] achieved 0.84 A cm^{-2} and Duan *et al.*[10] reached 0.74 A cm^{-2}, whereas the present work achieves 0.87 A cm^{-2} under the same applied voltage and temperature. These results suggest the processing technique mentioned above and the efficacy of the NiO-SZCY541-mediated sintering of the electrolyte at lower temperatures are highly effective in improving the performance of PCECs and their potential operation at lower temperatures. The amount of hydrogen gas produced during the electrolysis operation was quantified by gas chromatography. The evolved hydrogen rate follows Faraday's law and is proportional to the current density, exhibiting faradaic efficiencies close to 90% (Fig. S6, ESI†) for the BZCY44362|NiO-SZCY541 based cell and 85% for the BZCY44362|NiO-BZCY44362 cell. The deviations at higher current densities are ascribed to intrinsic electronic leakage through the electrolyte, consistent with several other experimental investigations.[7–9,17,25] Because of concerns about the impact of Sr segregation on the electrolyte conductivity, the behavior of the electrolyte conductivity with some amount of Sr doped in the A-site was investigated on sintered pellets. Fig. 5(e) and (f) show the ionic conductivity plot *versus* temperature and Sr content. As observed in Fig. 5(e), 10 mol% Sr-doped BZCY44362 exhibited nearly similar conductivity to pure BZCY44362 at 600 and 500 °C in wet air (P_{H_2O} = 1.9 × 10^3 Pa). However, as the Sr content in the A-site increased (Fig. 5(f)), there is a slight linear decrease in conductivity, although not significant. The electrochemical impedance spectroscopy (EIS) of the BZCY9144362 ($Ba_{0.9}Sr_{0.1}Zr_{0.44}Ce_{0.36}Y_{0.2}O_{3-\delta}$) based cell was evaluated in dry air (P_{O_2} = 0.21 atm), 20%, and 80% H_2O in the steam side electrode, with a 1% H_2 balance of Ar (99%) in the fuel side electrode. Increasing the steam pressure from 20% to 80% also enhances the electrode reaction, which is evidenced by the decrease in the EIS and the improvement in the IV characteristics, as shown in Fig. 5(g) and (h).

Furthermore, the long-term durability of the cell was examined at a constant current density of 0.5 A cm^{-2} at 600 °C, as illustrated in Fig. 6(a), with the 10 mol% Sr doped BZCY9144362

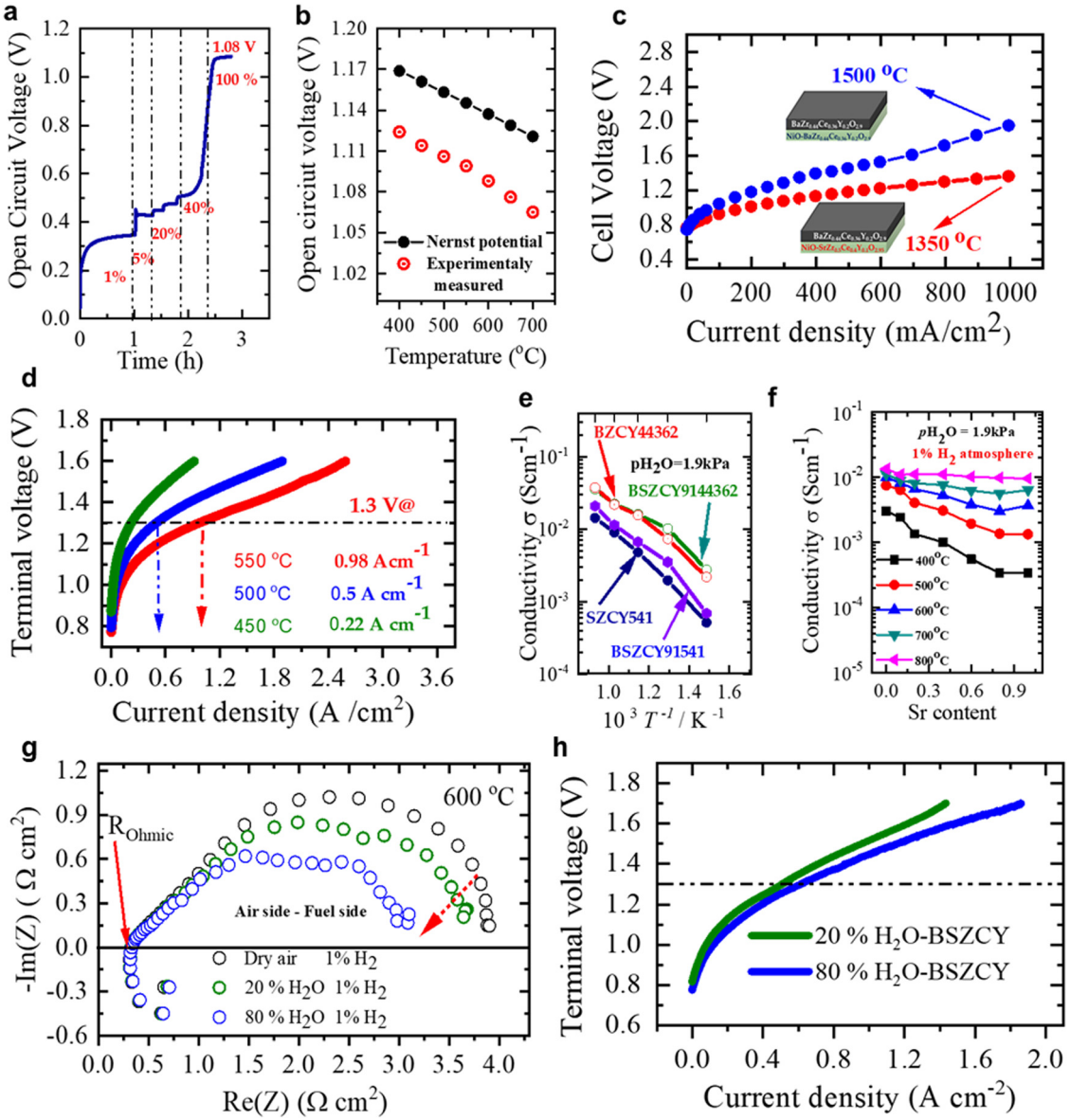

Fig. 5 (a) Open circuit voltage profiles measured during NiO reduction at 600 °C (b) experimentally measured and the corresponding theoretically calculated OCV values at different temperatures (c) comparison of the *I–V* curves of the BZCY44362|NiO-BZCY44362 and BZCY44362|NiO-SZCY541 based cell sintered at 1500 and 1350 °C respectively. (d) Typical *I–V* characteristics for a steam electrolysis cell based on BZCY44362|NiO-SZCY541 half-cell. (e) Comparison of the ionic conductivities of BZCY44362, $Ba_{0.9}Sr_{0.1}Zr_{0.44}Ce_{0.36}Y_{0.2}O_{3-\delta}$, (BSZCY9144362, SZCY541), and $Ba_{0.9}Sr_{0.1}Zr_{0.5}Ce_{0.4}Y_{0.1}O_{3-\delta}$ (BSZCY91541) in humid air. (f) Total electrical conductivity isotherms of B_xS_{1-x}ZCY9144362 in humid air. (g) Electrochemical impedance spectroscopy (EIS) of BLC|BSZCY9144362|NiO-SZCY541 cells measured with dry air (pO_2 = 0.21 atm), 20% H_2O, and 80% H_2O in the steam side electrode and 1% H_2 balance Ar (99%) in the fuel side. (h) *IV* characteristics of the BSZCY9144362-based cell with 20% and 80% H_2O on the airside and 1% H_2 on the fuel side.

($Ba_{0.9}Sr_{0.1}Zr_{0.44}Ce_{0.36}Y_{0.2}O_{3-\delta}$), electrolyte. The cell achieved a faradaic efficiency of about 85% and maintained its performance for over 1000 hours without any noticeable degradation or changes in the microstructure Fig. 6(c). Based on the later results, the calculated amount of electricity to produce 1 Nm^3 of H_2 is ~3.5 kW h within the as-measured durability range, as shown in Fig. 6(b).

3.4. Evidence of structural changes upon sintering at varying temperatures

To better understand structural changes in the half-cells upon sintering, we performed Raman mappings on the surfaces and cross-sections of half-cells sintered at 1300, 1350, and 1400 °C for 5 and 10 h dwell time. It is important to note that when exposed to elevated temperatures, the Raman spectra of BZCY-type oxides undergo structural changes, such as phase transitions or lattice distortions. Besides the latter, dopant ions turn to migrate and interact with the host lattice, thus leading to new Raman peaks or shifts in the existing peaks.

Fig. 7(a) presents the line average Raman spectra for a polished cross-section of a half-cell sintered at 1300 °C/10 h, illustrating the mapped area starting in the electrolyte at the top and extending into the fuel electrode below. The transition

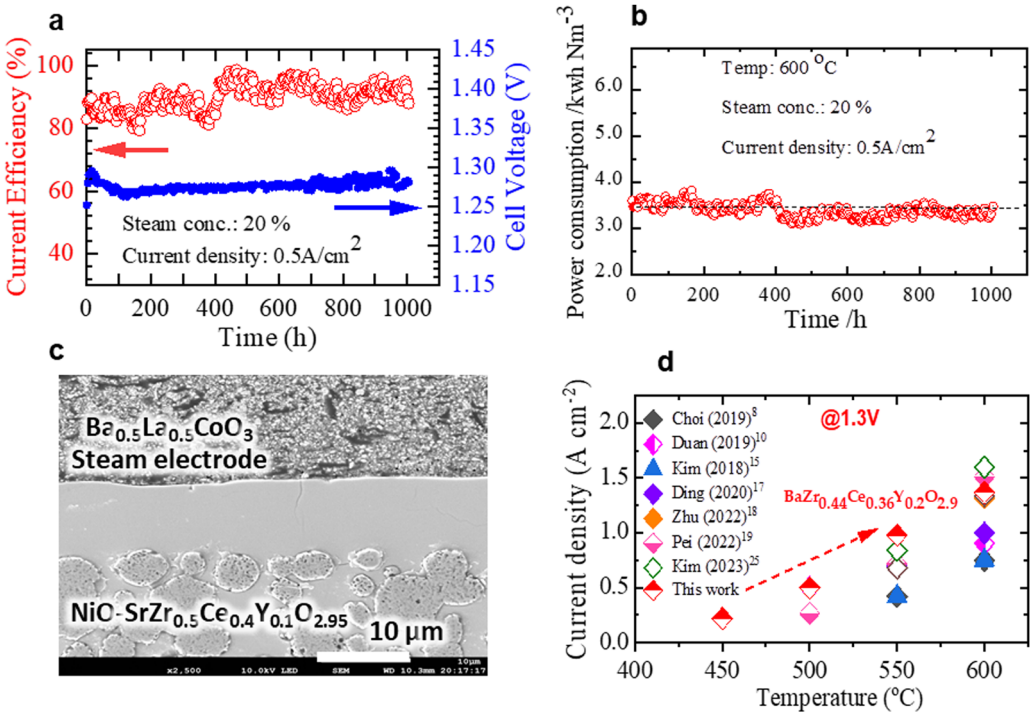

Fig. 6 (a) Long-term durability test of the BSZCY9144362-based cell at 600 °C. (b) Calculated amount of electricity to produce 1 N m^3 of H_2 as a function of time. (c) Microstructure of cell post measurement. (d) Performance comparison of our BZCY44362-based cell with similar electrolyte composition reported in the literature.

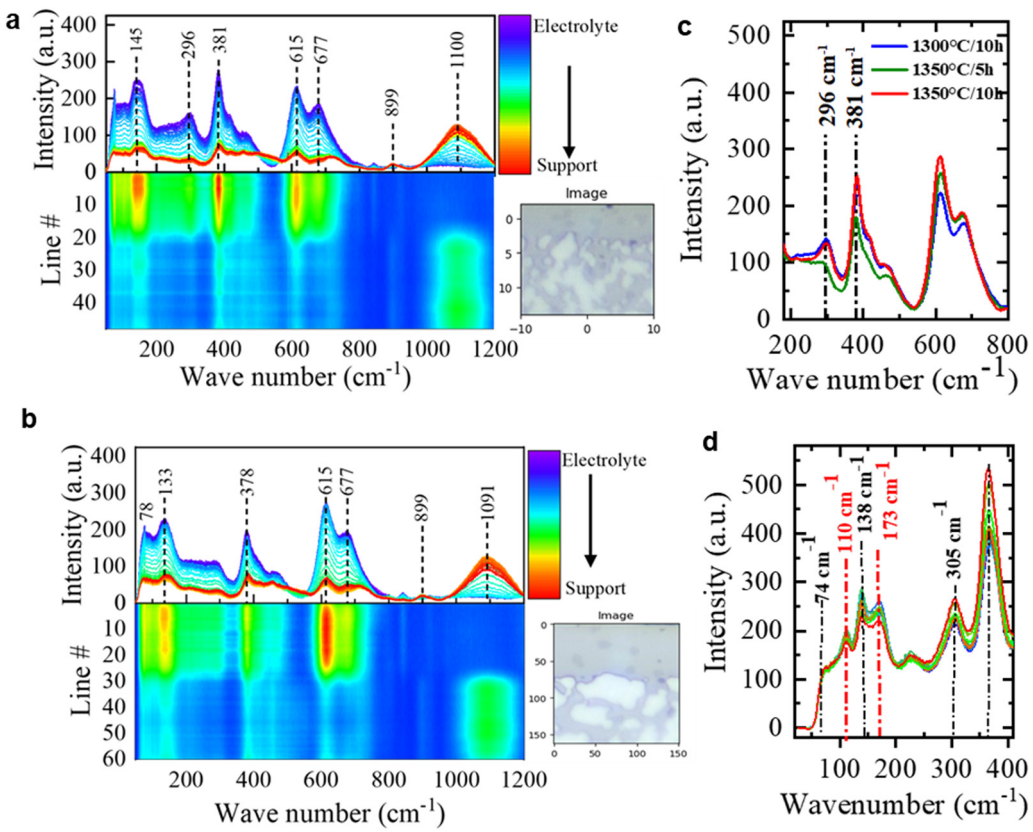

Fig. 7 Line averaged Raman spectra obtained from mapped areas of polished cross-sections of (a) BZCY44362|NiO-SZCY541 half-cell sintered at 1300 °C for 10 hours. (b) Polished cross-section of the half-cell sintered at 1350 °C for 5 hours the optical images. (c) Raman spectra from the electrolyte layer only, highlighting the well-resolved Y–O mode at 296 cm^{-1}. (d) Raman spectra from the polished cross-section of the half-cell sintered at 1400 °C.

between electrolyte and electrode is best seen in the rising Raman signal around 1100 cm^{-1}, which reflects the NiO in the fuel electrode. The spectra are characterized by peak positions typical of BZCY perovskite-type oxides.[26,27] Additionally, a well-resolved peak at ~296 cm^{-1} is observed in Fig. 7(b) and Fig. S8 (ESI†), which does not appear after a dwelling time of 5 hours, even following sintering at 1350 °C (see Fig. 7(c) and Fig. S7, ESI†). The modes around 74 and 145 cm^{-1} are associated with A-site cation ordering/symmetry primarily attributed to deformational motions and stretching vibrations of the Ba–[(Zr/Ce/Y)]O_6.[28–30] Upon sintering at 1400 °C, two distinct peaks at 110 and 173 cm^{-1} are observed, indicating structural changes within the Ba(Zr, Ce, Y)O_3 system, as shown in Fig. 7(d). These peaks are attributed to alterations in the Ba–O stretching and O–Ba–O bending modes, suggesting deviations from the electrolyte's ideal cubic symmetry (space group $Pm\bar{3}m$). Their appearance is related to local symmetry reduction due to Ba loss during sintering (see equation below) and Sr substitution in the A-site consistent with previous literature reports.[24,29,30] Furthermore, the Raman intensity of the X–O (X = Ce, Zr, Y) stretching mode around 615 cm^{-1} is significantly reduced and shifted, indicating a clear and definitive structural change in the material Fig. S11 (ESI†).

$$2Ba_{Ba}^{\times} + V_O^{\bullet\bullet} + Y_2O_3 \rightarrow 2Y_{Ba}^{\bullet} + O_O^{\times} + 2BaO$$

4. Conclusion

In summary, using a cost-effective sequential tape casting route, we have successfully fabricated flat, planar protonic electrolysis half-cells with impressive dimensions of up to 50 mm × 50 mm in size. The half-cells are constructed using NiO–$SrZr_{0.5}Ce_{0.4}Y_{0.1}O_{3-\delta}$ as the substrate, ensuring minimal warping and no cracks in the end-fired state and substantially promoting the half-cell's sintering activity at 1300 °C. The electrolyte is gas-tight with a He leakage rate well within the threshold necessary for cell operation (~5×10^{-5} hPa dm^3 (s $cm^2)^{-1}$). Using $Ba_{0.5}La_{0.5}CoO_{3-\delta}$ as the air electrode demonstrates remarkable capabilities and endurance within the 450–600 °C temperature range, as indicated by its current–voltage characteristics and hydrogen evolution rates. Our findings also show that upon sintering above 1350 °C, the electrolyte material undergoes evident structural changes with new defects that affect the perovskite host. This is highlighted by a progressive increase in the Raman relative intensity of the characteristic Y–O stretching vibration at 296 cm^{-1} from the electrolyte/electrode interface of the half-cell deep into the electrolyte with a sintering dwelling time of 10 h, providing evidence of local symmetry reduction due to Ba evaporation. Finally, these findings pave a possible path for low-cost fabrication of planar-type proton-conducting electrolysis cells.

Abbreviations

BZCY44362	$BaZr_{0.44}Ce_{0.36}Y_{0.2}O_{3-\delta}$
SZCY541	$SrZr_{0.5}Ce_{0.4}Y_{0.1}O_{3-\delta}$
BLC55	$Ba_{0.5}La_{0.5}CoO_3$

Author contributions

The manuscript was written with contributions from all authors. All authors have approved the final version of the manuscript.

Data availability

All relevant data are included within the manuscript and its ESI† files. The latter include tape-casting parameters, photographs and SEM images of the as-fabricated cells, Raman peak mapping and peak positions, *I–V* curves, hydrogen evolution rate, *etc.* (PDF).

Conflicts of interest

There are no conflicts to declare.

Acknowledgements

The authors gratefully acknowledge financial support through NEDO (International collaboration work in the field of clean energy) no.: 20001458-0, JSPS KAKENHI Grant-in-Aid for Scientific Research (C), no. 19K05672, the International Institute for Carbon-Neutral Energy Research (I2CNER) sponsored by the World Premier International Research Center Initiative (WPI), MEXT Japan and the Helmholtz Association of German Research Centres under the POF-MTET program.

References

1 S. D. Ebbesen, S. H. Jensen, A. Hauch and M. B. Mogensen, High-Temperature Electrolysis in Alkaline Cells, Solid Proton Conducting Cells, and Solid Oxide Cells, *Chem. Rev.*, 2014, **114**(21), 10697–10734, DOI: 10.1021/cr5000865.

2 M. van der Spek, C. Banet, C. Bauer, P. Gabrielli, W. Goldthorpe, M. Mazzotti, S. T. Munkejord, N. A. Røkke, N. Shah, N. Sunny, D. Sutter, J. M. Trusler and M. Gazzani, Perspective on the Hydrogen Economy as a Pathway to Reach Net-Zero CO_2 Emissions in Europe, *Energy Environ. Sci.*, 2022, **15**(3), 1034–1077, DOI: 10.1039/d1ee02118d.

3 R. W. Howarth and M. Z. Jacobson, How Green Is Blue Hydrogen?, *Energy Sci. Eng.*, 2021, **9**(10), 1676–1687, DOI: 10.1002/ese3.956.

4 D. Udomsilp, C. Lenser, O. Guillon and N. H. Menzler, Performance Benchmark of Planar Solid Oxide Cells Based on Material Development and Designs, *Energy Technol.*, 2021, **9**(4), 2001062, DOI: 10.1002/ente.202001062.

5 S. Wang, A. Inoishi, J. E. Hong, Y. W. Ju, H. Hagiwara, S. Ida and T. Ishihara, Ni–Fe Bimetallic Cathodes for Intermediate Temperature CO_2 Electrolyzers Using a $La_{0.9}Sr_{0.1}Ga_{0.8}Mg_{0.2}O_3$ Electrolyte, *J. Mater. Chem. A*, 2013, **1**(40), 12455–12461, DOI: 10.1039/c3ta11863k.

6 C. Lenser; D. Udomsilp; N. H. Menzler; P. Holtappels; T. Fujisaki; L. Kwati; H. Matsumoto; A. G. Sabato; F. Smeacetto; A. Chrysanthou and S. Molin, *Solid Oxide Fuel and Electrolysis Cells*, Elsevier Ltd., 2019, DOI: 10.1016/B978-0-08-102726-4.00009-0.

7 K. Leonard, Y. Okuyama, Y. Takamura, Y. S. Lee, K. Miyazaki, M. E. Ivanova, W. A. Meulenberg and H. Matsumoto, Efficient Intermediate-Temperature Steam Electrolysis with Y:$SrZrO_3$–$SrCeO_3$ and Y:$BaZrO_3$–$BaCeO_3$ Proton Conducting Perovskites, *J. Mater. Chem. A*, 2018, **6**(39), 19113–19124, DOI: **10.1039/c8ta04019b**.

8 S. Choi, T. C. Davenport and S. M. Haile, Protonic Ceramic Electrochemical Cells for Hydrogen Production and Electricity Generation: Exceptional Reversibility, Stability, and Demonstrated faradaic Efficiency, *Energy Environ. Sci.*, 2019, **12**(1), 206–215, DOI: **10.1039/c8ee02865f**.

9 K. Leonard, Y. Okuyama, M. E. Ivanova, W. A. Meulenberg and H. Matsumoto, Tailored and Improved Protonic Conductivity through $Ba(Z_xCe_{10-x})_{0.08}Y_{0.2}O_{3-\delta}$ Ceramics Perovskites Type Oxides for Electrochemical Devices, *ChemElectroChem*, 2022, **9**(4), 1–12, DOI: **10.1002/celc.202101663**.

10 C. Duan, R. Kee, H. Zhu, N. Sullivan, L. Zhu, L. Bian, D. Jennings and R. O'Hayre, Highly Efficient Reversible Protonic Ceramic Electrochemical Cells for Power Generation and Fuel Production, *Nat. Energy*, 2019, **4**(3), 230–240, DOI: **10.1038/s41560-019-0333-2**.

11 K. Leonard, Y. S. Lee, Y. Okuyama, K. Miyazaki and H. Matsumoto, Influence of Dopant Levels on the Hydration Properties of SZCY and BZCY Proton Conducting Ceramics for Hydrogen Production, *Int. J. Hydrogen Energy*, 2017, **42**(7), 3926–3937, DOI: **10.1016/j.ijhydene.2016.10.120**.

12 K. D. Kreuer, E. Schönherr and J. Maier, Proton and Oxygen Diffusion in BaCeO3 Based Compounds: A Combined Thermal Gravimetric Analysis and Conductivity Study, *Solid State Ionics*, 1994, **70–71**(Part 1), 278–284, DOI: **10.1016/0167-2738(94)90323-9**.

13 C. Zuo, S. Zha, M. Liu, M. Hatano and M. Uchiyama, $Ba(Zr_{0.1}Ce_{0.7}Y_{0.2})O_{3-\delta}$ as an Electrolyte for Low-Temperature Solid-Oxide Fuel Cells, *Adv. Mater.*, 2006, **18**(24), 3318–3320, DOI: **10.1002/adma.200601366**.

14 H. Zhu, S. Ricote, C. Duan, R. P. O'Hayre and R. J. Kee, Defect Chemistry and Transport within Dense $BaCe_{0.7}Zr_{0.1}Y_{0.1}Yb_{0.1}O_{3-\delta}$ (BCZYYb) Proton-Conducting Membranes, *J. Electrochem. Soc.*, 2018, **165**(10), F845–F853, DOI: **10.1149/2.1091810jes**.

15 J. Kim, A. Jun, O. Gwon, S. Yoo, M. Liu, J. Shin, T. H. Lim and G. Kim, Nano Energy Hybrid-Solid Oxide Electrolysis Cell: A New Strategy for e Ffi Cient Hydrogen Production, *Nano Energy*, 2018, **44**, 121–126, DOI: **10.1016/j.nanoen.2017.11.074**.

16 K. Leonard, J. Druce, V. Thoreton, J. A. Kilner and H. Matsumoto, Exploring Mixed Proton/Electron Conducting Air Electrode Materials in Protonic Electrolysis Cell, *Solid State Ionics*, 2018, **319**, 218–222, DOI: **10.1016/j.ssi.2018.02.016**.

17 H. Ding, W. Wu, C. Jiang, Y. Ding, W. Bian, B. Hu, P. Singh, C. J. Orme, L. Wang, Y. Zhang and D. Ding, Self-Sustainable Protonic Ceramic Electrochemical Cells Using a Triple Conducting Electrode for Hydrogen and Power Production, *Nat. Commun.*, 2020, **11**, 1907, DOI: **10.1038/s41467-020-15677-z**.

18 F. Zhu, F. He, D. Liu, H. Zhang, Y. Xu, K. Xu and Y. Chen, A Surface Reconfiguration of a Perovskite Air Electrode Enables an Active and Durable Reversible Protonic Ceramic Electrochemical Cell, *Energy Storage Mater.*, 2022, **53**, 754–762, DOI: **10.1016/j.ensm.2022.10.009**.

19 K. Pei, Y. Zhou, K. Xu, H. Zhang, Y. Ding, B. Zhao, Y. Choi, Y. Chen and M. Liu, Surface Restructuring of a Perovskite-Type Air Electrode for Reversible Protonic Ceramic Electrochemical Cells, *Nat. Commun.*, 2022, 1–10, DOI: **10.1038/s41467-022-29866-5**.

20 K. Leonard, W. Deibert, M. E. Ivanova, W. A. Meulenberg, T. Ishihara and H. Matsumoto, Processing Ceramic Proton Conductor Membranes for Use in Steam Electrolysis, *Membranes*, 2020, **10**(11), 1–18, DOI: **10.3390/membranes10110339**.

21 L. Q. Le, C. H. Hernandez, M. H. Rodriguez, L. Zhu, C. Duan, H. Ding, R. P. O'Hayre and N. P. Sullivan, Proton-Conducting Ceramic Fuel Cells: Scale up and Stack Integration, *J. Power Sources*, 2021, **482**, 228868, DOI: **10.1016/j.jpowsour.2020.228868**.

22 M. Marrony, M. Ancelin, G. Lefevre and J. Dailly, Elaboration of Intermediate Size Planar Proton Conducting Solid Oxide Cell by Wet Chemical Routes: A Way to Industrialization, *Solid State Ionics*, 2015, **275**, 97–100, DOI: **10.1016/j.ssi.2015.02.002**.

23 H. Matsumoto; K. Leonard; T. Fujisaki and K. Miyazaki, Steam Electrolysis Cells that Can Operate at 600 °C, in *CO_2 Free Ammonia as an Energy Carrier, ed. K.-i Aika and H. Kobayashi,* Springer Nature, Singapore, 2023. , DOI: **10.1007/978-981-19-4767-4**.

24 Y. Okuyama, K. Isa, Y. Sung, T. Sakai and H. Matsumoto, Incorporation and Conduction of Proton in $SrCe_{0.9-x}Zr_xY_{0.1}O_{3-\delta}$, *Solid State Ionics*, 2015, **275**, 35–38, DOI: **10.1016/j.ssi.2015.01.010**.

25 J. H. Kim, D. Kim, S. Ahn, K. J. Kim, S. H. Jeon, D.-K. Lim, J. K. Kim, U. Kim, H.-N. Im, B. Koo, K. T. Lee and W. C. Jung, An Universal Oxygen Electrode for Reversible Solid Oxide Electrochemical Cells at Reduced, *Energy Environ. Sci.*, 2023, **16**, 3803–3814, DOI: **10.1039/d2ee04108a**.

26 C. Tu, R. R. Chien, V. H. Schmidt, S. C. Lee and C. Huang, Temperature-Dependent Structures of Raman Scattering and X-Ray Diffraction, *J. Phys.: Condens. Matter*, 2012, **24**, 155403, DOI: **10.1088/0953-8984/24/15/155403**.

27 M. Karlsson, A. Matic, C. S. Knee, I. Ahmed, S. Eriksson and B. Lars, Short-Range Structure of Proton Conducting Perovskite Short-Range Structure of Proton-Conducting Perovskite $BaIn_xZr_{1-x}O_{3-x}/2$ (x = 0–0.75), *Chem. Mater.*, 2008, **20**, 3480–3486, DOI: **10.1021/cm7025448**.

28 P. Y. Bazro, F. Giannici, M. Shirpour, A. Longo, A. Martorana, R. Merkle and J. Maier, Long-Range and Short-Range Structure of Proton-Conducting Y: $BaZrO_3$, *Chem. Mater.*, 2011, **23**(11), 2994–3002, DOI: **10.1021/cm200682d**.

29 A. Slodczyk, P. Colomban, S. Willemin, O. Lacroix and B. Sala, Indirect Raman Identification of the Proton Insertion in the High-Temperature [Ba/Sr][Zr/Ti]O_3-Modified Perovskite Protonic Conductors, *J. RamanSpectrosc*, 2009, **40**, 513–521, DOI: **10.1002/jrs.2157**.

30 S. N. Shkerin, A. V. Rudakova, K. M. Bulanin and A. S. Khaliullina, ScienceDirect Raman Spectroscopy of $SrZrO_3$ Based Proton Conducting Electrolyte: Effect of Y-Doping and Sr-Nonstoichiometry, *Int. J. Hydrogen Energy*, 2020, **46**(32), 17007–17018, DOI: **10.1016/j.ijhydene.2020.11.236**.